Showcasing research from Professor Alexandru Vlad's laboratory, School of Chemistry, University of UCLouvain, Louvain-la-Neuve, Belgium.

Amorphous coordination polymers for versatile Mg^{2+}, Ca^{2+}, Sr^{2+}, Ba^{2+}, and Zn^{2+} cation storage

Developing sustainable, high-energy-density batteries is key for future energy storage. Divalent metal-ion systems, especially Mg and Ca, promise high volumetric capacity, low cost, safety, and sustainability, but progress is limited by the lack of high-performance positive electrodes. We introduce amorphous coordination polymers as electrodes for Mg, Ca, Sr, Ba, and Zn storage, achieving high voltages, stable cycling, and minimal hysteresis without solvent or anion co-intercalation. Their disordered frameworks weaken cation binding and enable fast diffusion, offering abundant, non-toxic materials for next-generation sustainable batteries.

Image reproduced by permission of Robert Markowski from *Energy Environ. Sci.*, 2025, **18**, 9114.

As featured in:

See Jan Bitenc, Jiande Wang, Alexandre Ponrouch, Alexandru Vlad *et al.*, *Energy Environ. Sci.*, 2025, **18**, 9114.

Check for updates

Amorphous coordination polymers for versatile Mg²⁺, Ca²⁺, Sr²⁺, Ba²⁺, and Zn²⁺ cation storage

Xiaolong Guo,†[a] Robert Markowski,†[a] Ashley Black,†[b] Petru Apostol,[a] Darsi Rambabu,[a] Olivera Lužanin,[c] Tjaša Pavčnik,[c] Damien Monti,[b] Mengyuan Du,[a] Da Tie,[a] Xiaodong Lin, [ID][a] Vasudeva Rao Bakuru,[a] Raphaël Delogne,[a] Koen Robeyns, [ID][a] Laura Simonelli, [ID][d] Jean-François Gohy, [ID][a] Jan Bitenc, [ID]*[c] Jiande Wang,*[a] Alexandre Ponrouch [ID]*[be] and Alexandru Vlad [ID]*[a]

Divalent metal-ion batteries hold immense promise for electrochemical energy storage applications, offering advantages in terms of volumetric capacity, cost-efficiency, sustainability, and safety. Despite advances, the lack of high-voltage and high-performance positive electrode materials remains a critical obstacle. Here, we disclose a family of amorphous coordination polymers capable of reversibly storing Mg²⁺, Ca²⁺, Sr²⁺, Ba²⁺, and Zn²⁺ cations. For Ca²⁺ and Mg²⁺ systems, the highest reported working potentials of >3.2 V *vs.* Ca²⁺/Ca and 2.8 V *vs.* Mg²⁺/Mg are measured, along with fast, stable, and low-hysteresis storage without solvent or ion pair storage. These characteristics stem from the amorphous structure, delocalized anionic charge, and disordered, long bond-distance coordination, enabling weak binding and fast cation diffusion. Using sustainable elements and demonstrating universal divalent cation storage capacity by achieving the first-ever reversible storage of Sr²⁺ and Ba²⁺ ions, this work establishes key design principles for divalent cation storage materials and systems.

Broader context

Developing high-energy-density, sustainable battery chemistries is essential for the future of electrochemical energy storage. Divalent metal-ion batteries offer advantages in volumetric capacity, cost-efficiency, sustainability, and safety, yet their progress is constrained by the scarcity of high-voltage, high-performance positive electrode materials. Magnesium (Mg) and calcium (Ca) batteries are among the most promising alternatives to lithium-ion systems, but their development is hindered by strong interactions between divalent cations and rigid inorganic hosts, which limit ion mobility and reversibility. While electrolyte design has advanced, the positive electrode remains a critical bottleneck. Here, we introduce amorphous coordination polymers as positive electrode materials for Mg, Ca, Sr, Ba, and Zn-ion storage, achieving high working potentials, stable cycling, and minimal voltage hysteresis. These electrodes store pure Mg²⁺, Ca²⁺, Sr²⁺, Ba²⁺, and Zn²⁺ without solvent or anion co-intercalation. Their favorable electrochemical properties arise from the synergy of delocalized anionic charge, disordered cation coordination, and the structural adaptability of an amorphous framework, which together weaken metal-ion binding and promote rapid diffusion. Composed of non-toxic, earth-abundant elements, these materials provide guiding principles for designing next-generation divalent metal-ion batteries and advancing sustainable, high-performance energy-storage technologies.

[a] *Institute of Condensed Matter and Nanosciences, Molecular Chemistry, Materials and Catalysis, Université catholique de Louvain, Louvain-la-Neuve B-1348, Belgium. E-mail: jiande.wang@uclouvain.be, alexandru.vlad@uclouvain.be*

[b] *Institut de Ciència de Materials de Barcelona, ICMAB-CSIC, Campus UAB, Bellaterra, Catalonia 08193, Spain. E-mail: aponrouch@icmab.es*

[c] *National Institute of Chemistry, Hajdrihova 19, 1000 Ljubljana, Slovenia. E-mail: jan.bitenc@ki.si*

[d] *ALBA Synchrotron Light Facility, Carrer de la Llum 2-26, Cerdanyola del Vallès, 08290, Spain*

[e] *ALISTORE-European Research Institute, CNRS FR 3104, Hub de l'Energie, Rue Baudelocque, Amiens 80039, France*

† These authors contributed equally to this work.

Introduction

Divalent metal batteries (DMBs) have garnered significant attention over the past few years as sustainable alternatives to lithium-based batteries.[1–3] Beyond the expected economic and environmental advantages,[4–6] DMBs offer higher volumetric capacity[3,4] and have the potential to address the safety concerns associated with lithium or sodium metal batteries,[7–9] making them promising candidates for next generation energy storage systems. This combination of sustainability, cost-effectiveness, and safety features underscores the transformative potential of DMBs in advancing energy storage technologies. However, despite steady progress in electrolyte formulations and metal

9114 | *Energy Environ. Sci.*, 2025, **18**, 9114–9124

This journal is © The Royal Society of Chemistry 2025

interphase stabilization, the development of efficient positive electrode materials remains a critical challenge.[6,10,11] This is compounded by several key issues: (i) poor performances arising from host–guest thermodynamic and crystallographic mismatches, driven by the higher coordination number of Ca^{2+} and Mg^{2+};[12–15] (ii) sluggish kinetics and large polarization caused by the strong electrostatic binding of divalent cations with the host structure, as well as solvent and anion co-intercalation;[11,16] and (iii) structural distortion and damage during cycling induced by cell volume variations upon repeated insertion and extraction of divalent cations.[16,17]

Positive electrode materials generally fall into two compositional classes: inorganic and organic structures. The former are known for their high stability and elevated working redox potential for mono-valent cation storage, but have thus far failed to deliver suitable performances for divalent cation storage due to their compact, rigid framework and high migration barrier for highly polarizing divalent cations.[18–25] Conversely, organic materials offer better lattice flexibility during charge and discharge, easy tunability of specific capacity, and reliance on abundant elements. However, they are often plagued by solubility issues, low working potentials, and a tendency to swell in the electrolyte, and thus store cation–anion paired or cation-solvated species, which diminishes their true performance metrics.[26–33] Numerous materials from both inorganic and organic classes have been investigated for Ca^{2+} and Mg^{2+} storage (Fig. 1), yet none have demonstrated simultaneously low hysteresis, high discharge voltage, high capacity, and good kinetics. Furthermore, most developed materials are synthesized in the oxidized, cation-free state, which is less practical for real-world applications.[11,34]

Recognizing the strengths of both inorganic and organic materials, we sought to combine these advantages by focusing on solid amorphous coordination polymers (CPs). Similar compositions have already been proven to be efficient for monovalent cation storage,[28] yet their compatibility with divalent cation storage has remained uncertain, as the transition to divalent ion storage systems is far from being a straightforward extrapolation, even when using the best-performing phases for Li-ion storage. The family of divalent-cation-containing conjugated CPs studied here were synthesized in their reduced (cation-reservoir) form *via* an acid–base reaction followed by cation exchange reactions (Fig. 2A), yielding compositions with the general formula DI–M–PTtSA. The CP combinations explored include DI storage cations such as Mg^{2+}, Ca^{2+}, Sr^{2+}, Ba^{2+}, or Zn^{2+}; M nodal metals such as Zn^{2+}, Co^{2+}, Ni^{2+}, Mn^{2+}, or Fe^{2+}; and the $PTtSA^{4-}$ Wurster-type redox center benzene-1,2,4,5-tetra-methylsulfonamide (Fig. 2B). Among these, the Mg/Ca–Zn–PTtSA compositions exhibited the best performance for Ca^{2+} and Mg^{2+} storage (Fig. 2B), achieving working potentials as high as 3.2 V *vs.* Ca^{2+}/Ca and 2.8 V *vs.* Mg^{2+}/Mg. Coupled with very low intrinsic hysteresis, these results mark a new milestone for Mg- and Ca-ion electrode chemistries (Fig. 1 and Table S1). Moreover, as the first materials capable of reversibly storing Sr^{2+} and Ba^+ ions (Fig. 2B), these coordination polymers establish DI–Zn–PTtSA as the first and the only reported universal framework for divalent cation storage. These remarkable properties arise from a synergy of factors, including the amorphous solid polymer phase, the highly reversible redox of the sulfonamide unit, and the inductive polarization effect of the nodal metals. Advanced *ex situ* and *operando* structural and compositional analyses revealed the charge storage mechanism, emphasizing pure divalent charge storage without coordinated solvents or salt anions. This work not only introduces the first highly efficient divalent-cation-containing materials for broad-spectrum divalent cation storage but also elucidates critical design criteria essential for high-performance next-generation DMBs.

Structural elucidation

The synthesis of DI–M–PTtSA materials relies on a general one-pot reaction, resulting in featureless particles with an agglomerate morphology (Fig. 2A and Fig. S1, Tables S2, S3). Elemental analysis (C, H, N, and S) and inductively coupled plasma optical emission spectroscopy confirmed the targeted composition of DI–M–PTtSA (Table S4). The proposed structure of DI–TM–PTtSA coordination polymers is presented in Fig. 2C. Since all synthesized DI–M–PTtSA materials exist as amorphous phases
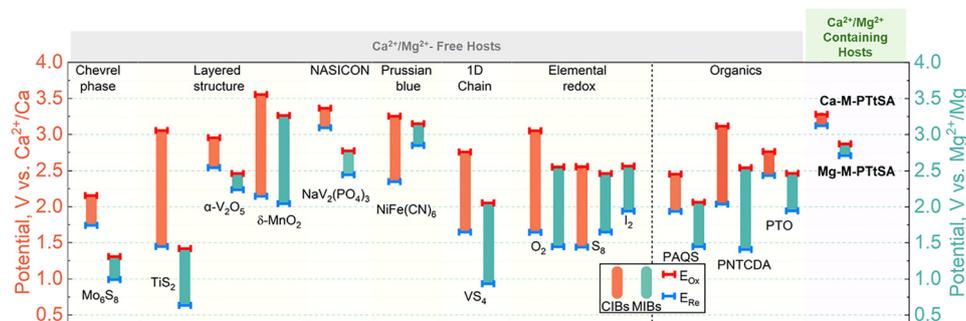

Fig. 1 Electrochemical characteristics of state-of-the-art divalent positive electrode materials. Comparison of DI–M–PTtSA materials developed in this work with leading materials studied to date for Mg^{2+} and Ca^{2+} storage, based on average oxidation–reduction potential values and hysteresis (the details of comparison analysis are given in Table S1). Legend: CIBs, calcium-ion battery materials; MIBs, magnesium-ion battery materials; E_{Ox}, average oxidation potential; E_{Re}, average reduction potential.

This journal is © The Royal Society of Chemistry 2025

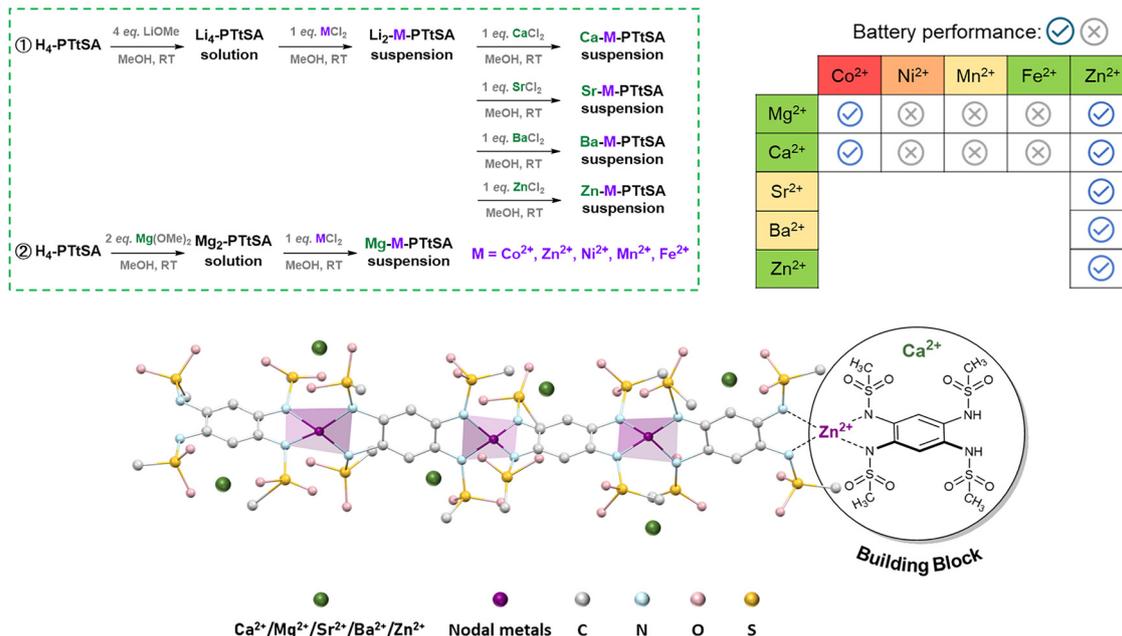*Energy Environ. Sci.*, 2025, **18**, 9114–9124 | 9115

Fig. 2 Synthesis and composition of developed divalent positive electrode materials DI−M−PTtSA. (A) Schematic representation of the synthetic routes for DI−M−PTtSA CPs explored in this work. Fixed-framework nodal metal cations are shown in purple (*e.g.* Co^{2+}, Zn^{2+}, Ni^{2+}, Mn^{2+}, and Fe^{2+}), while charge carrier cations (*e.g.* Mg^{2+}, Ca^{2+}, Sr^{2+}, Ba^{2+}, and Zn^{2+}) are highlighted in green. (B) Comparison of the synthesized DI−M−PTtSA compositions in terms of achieved battery performances and estimated environmental sustainability, with red indicating low sustainability and green denoting high sustainability. (C) Structural diagram of the conjugated coordination polymer DI−M−PTtSA as deduced from structural analysis.

(Fig. S2), direct structural elucidation using X-ray diffraction was not feasible. This complexity is further heightened by the presence of two distinct divalent cations with different environments, coordination modes, and a possible impact on electrochemical behavior. To address these challenges, we employed complementary indirect methods for structural elucidation.

Mononuclear complexes were synthesized and the structure was confirmed through single-crystal X-ray analysis (Scheme S1 and Tables S5–S7). These were subsequently used as model systems to probe the local structure of DI−M−PTtSA *via* synchrotron-sourced X-ray absorption near-edge structure (XANES) and extended X-ray absorption fine structure (EXAFS)

techniques. The mononuclear DI–M–(*o*-PDSA)$_2$ complexes, derived from the *N,N*-(1,2-phenylene)dimethanesulfonamide (H$_2$-*o*-PDSA) ligand, closely resemble half of the PTtSA ligand (Scheme S1). The excellent overlap of the sulfonamide band positions in the Fourier-transform infrared spectroscopy (FTIR) spectra between the polymer and the mononuclear complex (Fig. S3 and S4) suggests highly similar bonding modes, supporting the inference that DI−M−PTtSA shares the same metal coordination environment as the mononuclear complex (Fig. S5, S6 and Tables S5–S7).

Taking Ca–Co–PTtSA as a representative example, an identical XANES signature to that of the crystalline mononuclear Ca–Co–(*o*-PDSA)$_2$ complex is noted (Fig. 3A), implying an
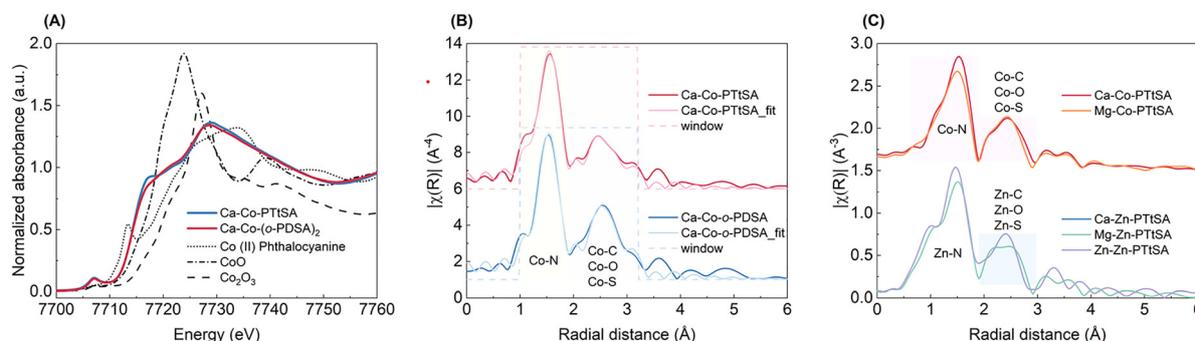

Fig. 3 Structural analysis. (A) X-ray absorption near-edge structure (XANES) for Ca−Co−PTtSA (red), mononuclear building block Ca−Co−(*o*-PDSA)$_2$ (blue), and the reference structures (Co(II)-phthalocyanine, cubic rock salt CoO, and Co$_2$O$_3$; black dotted lines) at the cobalt K-edge. (B) Fourier transform of the k^2 weighted extended X-ray absorption fine structure (FT-EXAFS) spectra along with the corresponding fitted results for Ca−Co−PTtSA and Ca−Co−(*o*-PDSA)$_2$ at the cobalt K-edge. (C) Comparison of FT-EXAFS spectra of most representative DI−M−PTtSA materials.

9116 | *Energy Environ. Sci.*, 2025, **18**, 9114–9124

This journal is © The Royal Society of Chemistry 2025

analogous Co^{2+} local structure. Both exhibit a strong pre-edge peak at 7707 eV, indicative of the 1s → 3d transition. This characteristic peak suggests a deviation from the centrosymmetric geometry and a notable 3d-4p mixing, aligning with a distorted and disordered tetrahedral coordination environment around the Co^{2+} center. Single crystal analysis confirms a distorted tetrahedral geometry (with a CN = 4) for Ca–Co–(o-PDSA)$_2$, with N1–Co–N2 dihedral angles of 82° and 125° (Fig. S5 and Tables S5, S6). Given the similar XAS spectra, we infer that Ca–Co–PTtSA exhibits the same tetrahedral configuration. Square planar geometry was ruled out by comparison with Co(II) phthalocyanine spectra, while the absence of high-intensity pre-edge peaks, multiple 1s → 3d transitions, edge shifts, and complex post-edge features rules out the rare cubic four-coordinate geometry for Ca–Co–PTtSA (Fig. 3A and Fig. S7). The Co K rising edges' energy positions were found to be compatible with the Co^{2+} oxidation state in both cases, as compared to the references (CoO and Co_2O_3). Building upon this, a detailed analysis was performed by modeling the Fourier-transformed (FT) k^2-weighted EXAFS data signal in a single scattering approximation (Fig. 3B). The results reveal that the local structure around Co^{2+} in both the Ca–Co–PTtSA and mononuclear Ca–Co–(o-PDSA)$_2$ complexes is identical within the measurement error (Fig. S8 and Table S8). The model captures the first and second coordination shells, featuring four N atoms at approximately 1.996 Å, four C atoms around 2.92 Å, as well as both, short (around 3.12 Å) and long (around 3.2 Å) Co–O and Co–S distances (around 3.09 and 3.18 Å), depicting a distorted tetrahedral coordination geometry around the Co^{2+} centers.

Regarding the DI coordination environment, the Ca K-edge XAS analysis indicates two pre-edge features separated by ∼1 eV in the Ca–Co–PTtSA CP, in contrast to only one observed in the $CaSO_4$ reference sample (Fig. S9A). The 1 eV pre-peak splitting is the signature of 6 coordinated species and corresponds to the e_g-t_{2g} energy splitting. For 7–8 coordinated complexes, such a shift is not visible within the core–hole lifetime broadening.[35] This supports a coordination number of Ca^{2+} of 7–8 in $CaSO_4$ (Fig. S9B) and on average of 6 in Ca–Co–PTtSA.[35] Additionally, the FT k^2-weighted EXAFS spectral analysis is compatible with a preference for Ca^{2+} ions to selectively bind to O atoms of the $-SO_2-$ groups (Fig. S9C), in agreement with the HSAB principle. Given the absence of solvents in the Ca–Co–PTtSA phase (Fig. S3), the coordination of Ca^{2+} ions predominantly involves the oxygen atoms of the mesyl ($-SO_2-$) groups. This aligns with FTIR spectra showing a shift in the $-SO_2-$ stretching band to lower wavenumbers in Ca–Co–PTtSA compared to Li_2–Co–PTtSA (Fig. S10), indicating that Ca^{2+} coordination with $-SO_2-$ depletes electron density, lowering the S=O bond stretching energy. The visibility of only the first shell (Fig. S9C) also implies a relative disorder within the Ca–Co–PTtSA environment, providing further evidence of the disordered nature of these materials.

The Ca–Zn–PTtSA phase shares comparable structural features and binding modes with Ca–Co–PTtSA (Fig. 3C and Fig. S11, S12), revealing that these materials display analogous

structural and binding modes (Fig. S13 and Fig. 3C), consistent with the proposed structure for the 1D coordination polymer chain depicted in Fig. 2C. The M metal nodes are tetrahedrally (distorted) coordinated by the nitrogen atoms of the PTtSA^{4-} ligand, forming the polymer chain, with the DI cations required to maintain the charge balance. Essential for transport and storage, this analysis globally reveals a long-range disordered structure, a low coordination number for Ca^{2+} (6), high average Ca–ligand distances (2.4 Å), and partial negative charge on mesyl oxygen atoms, with Ca^{2+} (but also Mg^{2+}) thus weakly bound to the framework, resulting in a low diffusion energy barrier for transport and storage (refer next for details and discussion).

The divalent cation storage performances of DI–M–PTtSA electrode materials

Initial developments entailed the development of DI–M–PTtSA CP with Co^{2+} nodal metal as proof-of-concept exploration, demonstrating promising storage performances (Fig. S14). However, due to the sustainability concerns associated with Co^{2+}, it was successfully replaced by other nodal metals, such as Zn^{2+}, Ni^{2+}, Mn^{2+}, and Fe^{2+}. The divalent cation storage performance of the representative DI–Zn–PTtSA is summarized in Fig. 4. Given that the DI–Zn–PTtSA contains the charge storage divalent cations, and that the redox centers are in the reduced state (alike in conventional metal-ion positive electrode materials), the electrochemical characterization was initiated with the extraction of Mg^{2+}, Ca^{2+}, Sr^{2+}, Ba^{2+} or Zn^{2+} (i.e. oxidation or cell charge process). All materials demonstrating reversible storage of the respective contained DI cations (Fig. 4A and Fig. S15). It has to be emphasized that no material reported to date has shown ability to store five different divalent cations, establishing DI–Zn–PTtSA as the first universal divalent cation storage host. Notably, Sr–Zn–PTtSA and Ba–Zn–PTtSA are the only materials reported to enable reversible electrochemical storage of Sr^{2+} and Ba^{2+}, with the latter being for instance nearly twice the size of Mg^{2+}, yet still showing high efficiency in storage. The Ca–Zn–PTtSA phase developed herein is also the first reported Ca-ion-containing positive electrode material, exhibiting highly reversible Ca^{2+} extraction/uptake.[22,36,37] All other materials reported for Ca^{2+} storage are characterized by either low reversibility or high hysteresis or are prepared in the pristine oxidized state, which may limit the practical applicability (Fig. 1). Similarly, only a few electroactive Mg/Zn-ion containing materials are available, all nevertheless exhibiting low discharge voltage, high polarization, and low efficiency during charge–discharge cycles.[13,38] Given the promising potential of Ca–Zn–PTtSA and Mg–Zn–PTtSA for battery applications, their charge storage performances were further investigated in detail.

The galvanostatic charge–discharge curves of the Ca–Zn–PTtSA notably exhibit a reversible two-electron redox behavior, characterized by two pairs of sloping plateaus averaging at 3.24 V vs. Ca^{2+}/Ca (Fig. S16). For Mg-ion phases, the average
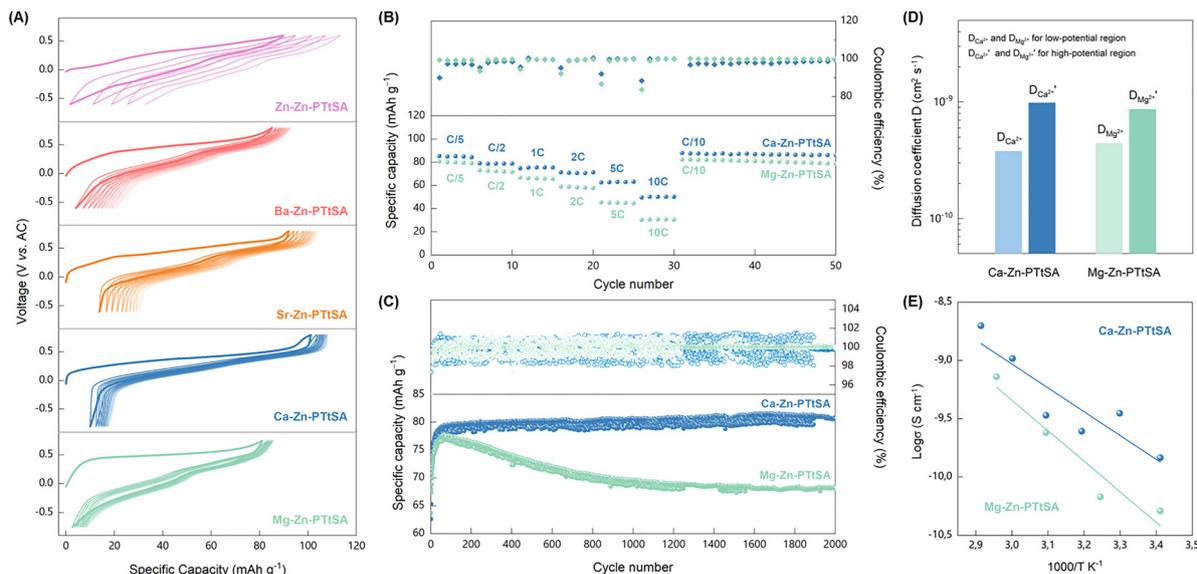
This journal is © The Royal Society of Chemistry 2025

Energy Environ. Sci., 2025, **18**, 9114–9124 | **9117**

Fig. 4 Divalent cation storage performances of the DI–M–PTtSA materials. (A) Galvanostatic voltage-capacity profiles for Mg/Ca/Sr/Ba/Zn–Zn–PTtSA acquired at a rate of C/10 (1C being equivalent of 100/97/89/82/93 mA g^{-1}, respectively). (B) Capacity retention at different cycling rates for Ca-ion and Mg-ion electrodes (1C is equal to 100 mA g^{-1} for Mg–Zn–PTtSA and 97 mA g^{-1} for Ca–Zn–PTtSA). (C) Long-term cycling performances of Mg/Ca–Zn–PTtSA cells cycled at a current density of 100 mA g^{-1} (or 1C rate). (D) Diffusion coefficients and (E) electrical conductivity of Ca– and Mg–Zn–PTtSA CPs. The electrolyte formulations used in (A) were 0.5 M Ca (TFSI)$_2$ DME for Ca^{2+}, 0.1 M Mg(ClO$_4$)$_2$ PC for Mg^{2+}, 0.5 M Sr(ClO$_4$)$_2$ ACN for Sr^{2+}, 0.5 M Ba(ClO$_4$)$_2$ ACN for Ba^{2+} and 0.5 M Zn(TFSI)$_2$ DME for Zn^{2+} storage.

redox potential is 2.81 V *vs.* Mg^{2+}/Mg (Fig. S17). In our previous study, adding a transition metal like Co^{2+} to form Li$_2$–Co–PTtSA also resulted in a two plateau electrochemical response (compared to a single plateau in the parent Li$_4$–PTtSA), indicating a sequential electron transfer.[27,28] This arises from TM-induced electron cloud delocalization, which stabilizes the semi-quinone type radical intermediate and enables stepwise electron transfer. The differential capacity (dQ/dV) plots (Fig. S18) confirm this mechanism, with distinct peaks corresponding to redox events and phase transformations occurring during cation exchange. ICP analysis further supports this two-electron process, showing that precisely 50% of the Ca^{2+} ions are removed in half-charge and half-discharge states. Similarly, in DI–M–PTtSA, the dual inclined platforms in the galvanostatic charge–discharge response (Fig. 4A) demonstrate a reversible, one-by-one, two electron redox behavior. The variations in the cycling profiles of DI–M–PTtSA CPs (Fig. 4A) result from a combination of factors, including the intrinsic properties of each electrode material, phase transformations during cycling, electrochemical kinetics, and electrolyte composition, influenced by the nature of the divalent cation (*i.e.* ionic radius and charge density). In addition, the working potential of DI–M–PTtSA ranks among the highest in both Ca-ion and Mg-ion electrode materials (Fig. 1), attributed to the synergistic effect of the intrinsically high redox potential of the sulfonamide functionality and the inductive polarization effect of the nodal metal (Co^{2+}, Zn^{2+}, *etc.*).[28]

Notably, compared to state-of-the-art Mg- and Ca-ion electrode materials, both Mg^{2+} and Ca^{2+} extraction and uptake in Mg/Ca–Zn–PTtSA occur with remarkably low polarization. Mg–Zn–PTtSA achieves a low voltage hysteresis of only 100 mV for

Mg^{2+} storage, rivaled only by a few materials like Chevrel phases, V$_2$O$_5$, or NASICON (Fig. S19 and Table S10). Ca–Zn–PTtSA attains a hysteresis of just 60 mV upon Ca^{2+} release and storage—the lowest reported to date—surpassing previously studied NASICON and FePO$_4$ phases (Fig. S19 and Table S11) and establishing these electrode materials as the most energy-efficient developed to date. The exceptionally low hysteresis in Ca/Mg–Zn–PTtSA is attributed to the structural factors: (i) the amorphous nature which creates a flexible framework capable of accommodating large cations and (ii) the weak interaction of the cations with the host framework, facilitated by electron delocalization throughout the organic components (as discussed in the Structural elucidation section). Even with larger cations such as Sr^{2+} and Ba^{2+}, the hysteresis remains low, around 70 mV (Fig. 4A).

The observed difference between the first cycle and subsequent charge steps is attributed to conformational rearrangements associated with the rotation of the methyl sulfonyl group, which is triggered by the extraction and reinsertion of divalent cations. The first charging cycle can be considered as an activation step, marked by the reorganization of both the polymer and the DI environment. This transformation is influenced by the polymer's solvation structural 'history' arising from the synthesis step, which subtly but significantly alters the structure of the pristine material compared to its state after electrochemical cycling. Our data suggest that this activation is an inherent property of the materials, stemming from the peculiar solvation and desolvation processes during the materials synthesis. This process, although not affecting the overall charge storage performances, is discussed in detail in Fig. S20 and S21 and Table S12.

9118 | *Energy Environ. Sci.*, 2025, **18**, 9114–9124

This journal is © The Royal Society of Chemistry 2025

Fig. 4B and C display the rate capability and long-term cycling performances of Ca–Zn–PTtSA and Mg–Zn–PTtSA electrodes. Taking Ca–Zn–PTtSA as an example, at a rate of 5C (with 1C rate being equivalent of $2e^-–1Ca^{2+}$ exchange in 1 hour, or 97 mA g^{-1}), nearly 70% of the nominal capacity is retained. Mg–Zn–PTtSA exhibits comparable rate performances, attributed to the intrinsic electronic conductivity (Fig. 4E and Fig. S22) and in particular to the divalent cation diffusion kinetics. Indeed, the diffusion coefficients extracted from the galvanostatic intermittent titration technique were found to range between 1.1×10^{-10} and 9.8×10^{-10} cm^2 s^{-1} (Fig. 4D and Fig. S23–S29, Table S13), which, compared to other reported materials,[39–42] represent outstanding dynamic properties. The average capacity retention rate per cycle is also excellent, considering the state-of-the-art achievements in divalent cation storage (Tables S10 and 11), with approximately 99.9% for Ca–Zn–PTtSA and 99.7% for Mg–Zn–PTtSA. Even after 2000 cycles, Ca–Zn–PTtSA and Mg–Zn–PTtSA retain 99% and 90% of their initial capacity, respectively (Fig. 4C). Moreover, at a high rate of 10C, no capacity fading is observed over 3000 cycles (Fig. S30). The localization and weak binding of Ca^{2+} and Mg^{2+} ions on the periphery of the coordination chain (refer to Fig. 2C and associated structural analysis) enable high mobility during the cycling process without perturbing the integrity of the backbone structure, thereby preserving the framework's stability. In addition, the electrode morphology is well preserved throughout cycling, as no significant differences were observed between the cycled and pristine electrodes in SEM images (Fig. S31), further highlighting the remarkable structural stability and dynamic integrity of these coordination polymers. The developed materials can also be used with a low carbon content (down to 10 wt% tested) and high mass loading (up to 10 mg cm^{-2} tested), and despite the minor decrease in material utilization, the DI–M–PTtSA CPs remain on top of the best-performing available Mg/Ca-ion storage materials (Fig. S32–S36). Other DI–M–PTtSA compositions (DI = Ca^{2+} and Mg^{2+}; M = Fe^{2+}, Mn^{2+}, and Ni^{2+}) were also synthesized and characterized (Fig. S37), with, however, the partial oxidation of nodal metals leading now to structure instability and solubility in the electrolyte (Fig. S38 and S39).

Overall, the electrochemical analysis of the disclosed DI–Zn–PTtSA phases highlights the remarkable versatility of these divalent-cation-containing coordination polymers as universal positive electrode materials for DMBs. They exhibit an exceptional balance of stability, energy density, and cyclability, setting a new benchmark in the field. While these coordination polymers may not claim the top position in any single performance metric, their overall cycling performance is outstanding, ranking them among the best across all key categories combined (Table S14).

Divalent cation storage mechanism

Due to the high ion association energy of divalent cations, their storage often involves solvent and anion co-intercalation, impacting electrode integrity and reducing the practical energy storage metrics.[11,25,43] Using Ca–Co–PTtSA and Ca–Zn–PTtSA as representative electrode materials, our examination in various states-of-charge (SOC) (Fig. 5A–C) shows a significant decline in the Ca/Co elemental ratio from 0.92 to 0.02 upon oxidation (cell charge and Ca^{2+} extraction), recovering to 0.96 after reduction (cell discharge and Ca^{2+} uptake). This confirms the selective shuttle of only calcium cations (Fig. 5B), excluding other potential species (i.e. protons,[44] anions,[45,46] or possible redox activity of the Co^{2+} metal node). Even after multiple cycles, the Ca/Zn atomic ratio remains at 0.93 and 0.92, after 50 and 100 cycles, respectively (Table S15), demonstrating the excellent robustness of these materials on extended cycling. The slight decrease in the cation ratio may be assigned to the small capacity fading observed over the cycles, attributed to a minor leaching of the oxidized ligand into the electrolyte (Fig. S40 and S41). Ex situ FTIR analysis revealed an identical vibrational fingerprint between pristine and cycled electrodes, confirming the quantitative chemical reversibility of the redox process (points I and V, Fig. 5C).[26–28] Ion chromatography consistently detected fluorine content below 1 wt%, indicating Ca^{2+} uptake free of ion pairs (for example, expected at 13.81 wt% F if CaTFSI$^+$ would be stored), with the detected fluorine traces stemming from electrolyte residues. Ex situ FTIR analyses also revealed no solvation of Ca^{2+} by DME during uptake (the absence of specific DME vibration bands in Fig. 5D), where the visible band around 3000 cm^{-1} is attributed to the C–H stretching vibrations of the aromatic and methyl groups present in the organic ligand framework. Similar results are noted for Mg–M–PTtSA, indicating pure Mg^{2+} cation storage (Fig. S42 and S43). These findings highlight that Ca/Mg–M–PTtSA CPs effectively store pure divalent cations without anion pairs or solvent molecules, while exhibiting a high rate and low hysteresis—a rare feature in divalent cation storage systems. Alike in the Mo$_6$S$_8$,[47,48] where Mo cations induce unpairing by acting on anions, Ca/Mg–M–PTtSA undergoes a similar mechanism, with nodal metals and mesyl groups playing a comparable role. This promotes the desolvation and ion pair dissociation, enabling the storage of pure divalent ions; however, further comprehensive studies are necessary to validate this hypothesis.

Fig. 5E displays operando XANES results for Ca–Co–PTtSA. The Co K-edge rising-edge energy position (7714 to 7719 eV) gradually shifts to higher energies during oxidation and exhibits perfect reversibility, shifting to lower energy during reduction. This indicates effective reversibility in electronic and structural environments during Ca^{2+} extraction and uptake, aligning with electrochemical cycling data (Fig. 4 and Fig. S44A). In contrast to pristine samples (Fig. 5F and G), the fully oxidized state exhibits a minor energy shift in the rising edge position of 0.4 and 0.3 eV for Ca–Co–PTtSA and Ca–Zn–PTtSA, respectively. This indicates the absence of Co^{2+}/Co^{3+} redox during the oxidation process, supported by the expected energy shift of up to 3.5 eV for the Co^{2+}–Co^{3+} transition (Fig. 2A).[49] These are also confirmed by XPS and molecular electrochemistry of model mononuclear building block analysis, which reveal that the Co^{2+} to Co^{3+} oxidation occurs 500 mV above the redox potential of the organic moiety (Fig. S45–S47). Such minor energy shifts are associated with structural variations upon redox of the PTtSA^{4-} ligand, where higher rising
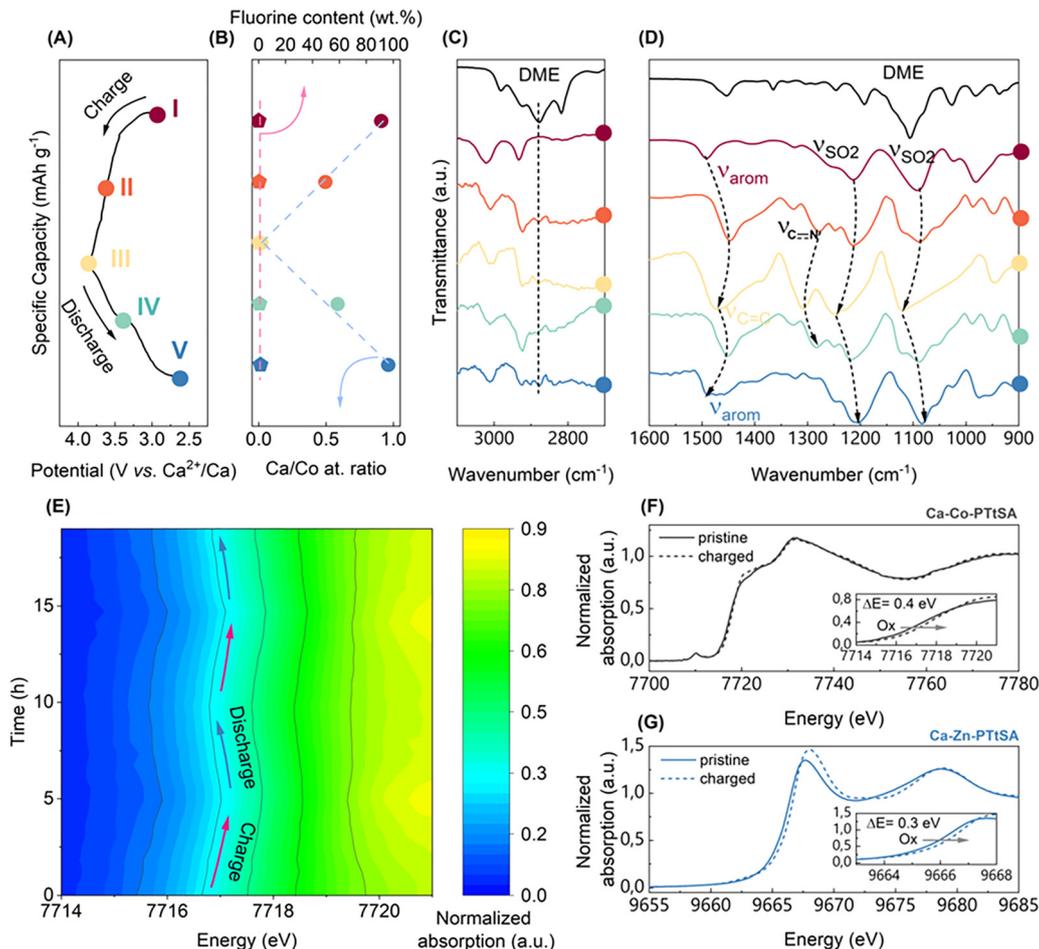
Fig. 5 *Ex situ* and *operando* analysis of the divalent cation storage mechanism in Ca−[Zn/Co]−PTtSA. (A) The galvanostatic charge−discharge curve with selected different Ca^{2+} containing states: pristine (I), one electron half-oxidized (II), two electrons fully oxidized (III), one electron half-reduced (IV), and two electrons fully reduced (V). The corresponding (B) *ex situ* elemental analysis results and (C) and (D) *ex situ* FTIR survey. (E) The contour plot of the *operando* XAS XANES region of Ca−Co−PTtSA for the initial two galvanostatic charge−discharge cycles acquired at a rate of C/10; the yellow and blue contours represent high and low adsorption intensities, respectively. (F) XAS spectra of pristine Ca−Co−PTtSA (solid line) and oxidized form (dotted line) at the cobalt K-edge. The inset shows an enlarged view of the 7714−7721 eV range. (G) XAS spectra of pristine Ca−Zn−PTtSA (solid line) and oxidized form (dotted line) at the zinc K-edge. The inset shows an enlarged view in the range of 9965 to 9968 eV.

edge energies suggest a contracted local structure. Additionally, the pre-edge feature of the Co K-edge XAS spectra, highly sensitive to metal coordination, remains constant during electrochemical cycles (Fig. S44B). This observation further supports no change in the Co oxidation state.

Operando XANES measurements for the Ca−Zn−PTtSA and Mg−[Zn/Co]−PTtSA also confirmed a fully reversible process (Fig. S48−S50). Notably, the Würster-type PTtSA$^{4−}$ ligand serves as the redox-active center, influencing the rising-edge position of the metal nodes during electrochemical cycling, which reflects local structural changes. In the analysis of local structural evolution during Ca^{2+} extraction and uptake in Ca−Co−PTtSA, the Co K-edge EXAFS spectra were fitted with the previously described mononuclear complex (Fig. S51 and Table S16). Following Ca^{2+} extraction, the first shell (Co−N bond distance) remains nearly constant, while the second shell exhibits a complex peak shift due to changes in Co single scattering events with C, O, and S atoms. The predominant feature

is a shift towards lower distances in Co−C interactions, attributed to C−N bond contraction (single to double C−N bond transition) within the ligand upon oxidation (Scheme S2), following the Wurster-type redox process.[26] This finding aligns with the redox process being centered on the ligand within the studied voltage range. In summary, upon oxidation, the PTtSA$^{4−}$ ligand undergoes a two-electron process, reducing its overall charge from −4 to −2. To maintain charge neutrality, one DI^{2+} cation is released from the coordination polymer. During reduction, the reverse process occurs, involving the reuptake of DI^{2+} cations into the polymer framework (Scheme S2).

Ca and Mg metal cells

As a proof of concept and motivated by the excellent storage performances of these materials, we assembled calcium- and magnesium-metal cells using the state-of-the-art and best
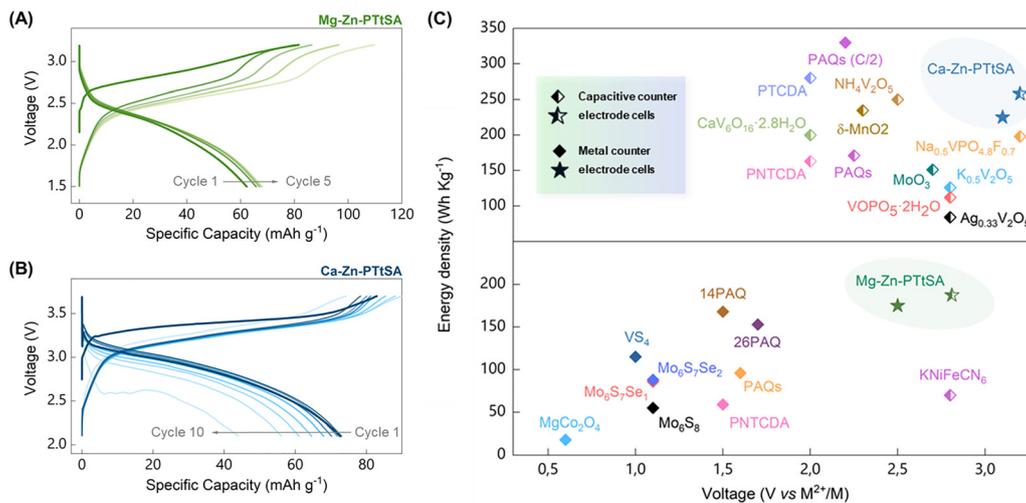
9120 | *Energy Environ. Sci.*, 2025, **18**, 9114–9124

This journal is © The Royal Society of Chemistry 2025

Fig. 6 Metal cell prototype and electrochemical characteristic comparison. Galvanostatic charge–discharge profiles of (A) the Mg metal – Mg–Zn–PTtSA cell prototype using 0.4 M Mg[Al(hfip)$_4$]$_2$ (magnesium tetrakis(hexafluoroisopropyloxy)aluminates) in the bis(2-methoxyethyl) ether electrolyte and (B) the Ca metal – Ca–Zn–PTtSA cell prototype using 0.4 M Ca[B(hfip)$_4$]$_2$ (calcium tetrakis(hexafluoroisopropyloxy)borate) in 1-2-dimethoxyethane, cycled at a rate of 1C (100 mA g^{-1}). (C) The specific discharge gravimetric energy density at a 1C rate as a function of average discharge voltage for Ca–Zn–PTtSA (top) and Mg–Zn–PTtSA (bottom) as compared to the reported positive electrode materials in metal and capacitive (with activated carbon as the counter electrode) cell configurations. The specific energy is calculated based on the average discharge potential (V vs. Ca^{2+}/Ca or Mg^{2+}/Mg) and specific discharge capacity (Ah kg^{-1}). All references are summarized in Tables S18 and S19. Capacitive cells are represented by half-filled symbols, whereas metal cells are denoted by fully filled symbols.

performing electrolytes available to date (Fig. 6A and B). In the case of Ca metal cells, the only reported compatible electrolytes are based on Ca[B(hfip)$_4$]$_2$ (calcium tetrakis(hexafluoroisopropyloxy)borate) or Ca[Al(hfip)$_4$]$_2$ (calcium tetrakis (hexafluoroisopropyloxy)aluminate) in ether solvents.[50] These electrolytes enable reversible Ca plating/stripping at room temperature and offer rather good anodic stability (>3 V vs. Ca^{2+}/Ca). However, similar to the case of reported poly(anthraquinonyl) sulfide (PAQs), the Ca metal–Ca–Zn–PTtSA cell (Fig. 6B) failed after 10 cycles due to the gradual formation of a passivation layer on the Ca metal surface, which impedes Ca^{2+} transport and prevents long-term Ca plating/stripping. Setting aside the issue of the passivation layer, Ca–Zn–PTtSA demonstrates cycling performance comparable to PAQs in Ca metal cells.[50] While it offers an apparent lower specific capacity, it operates at a significantly higher voltage.

For Mg metal cells, 0.6 M Mg[Al(hfip)$_4$]$_2$ in (bis(2-methoxyethyl)ether)[51] was found as the electrolyte formulation with the highest anodic stability (Fig. S52), with nevertheless the onset of anodic decomposition at 2.7 V vs. Mg^{2+}/Mg. However, the high voltage characteristic of Mg–Zn–PTtSA was found to be slightly beyond the thermodynamic anodic stability of this electrolyte, thus requiring a compromise between the active material utilization and cycling stability (Fig. S53). Upon electrode, electrolyte, and cycling condition optimization (Fig. S54), the Mg metal cells achieved 70% of the theoretical capacity with an average working voltage of 2.4 V (Fig. 6A), with, however, higher utilization resulting in lower efficiency due to decomposition of the electrolyte at the upper potential limit. FTIR and ICP analyses of cycled composite electrodes also confirmed that the Mg ions are neither solvated nor ion-paired within the coordination polymer, when cycled in this electrolyte

formulation as well, further emphasizing the versatility for pure solid-phase storage of divalent cations (Fig. S55 and Table S17).

Comparing DI–M–PTtSA to the reported positive electrode materials for divalent cation storage, we highlight the superior energy storage metrics in Fig. 6C (the details of the analysis are provided in Tables S18 and S19). In Mg systems, Mg–Zn–PTtSA competes closely with 1,4-polyanthraquinone (14PAQ) in Mg metal cells, offering slightly higher energy density and importantly operating at a significantly higher potential, approximately 1 V above that of 1,4-polyanthraquinone. Polyanthraquinones[52] are known to swell in the electrolyte, accommodating partially solvated cations and ion pairs. This process reduces the effective energy storage metrics, whereas in Mg–Zn–PTtSA, Mg^{2+} storage occurs strictly in the solid state. For Ca systems, Ca–Zn–PTtSA shows high performance in capacitive cells, where it delivers a higher voltage than 3,4,9,10-perylene tetracarboxylic dianhydride (PTCDA), despite the slightly lower energy density. In Ca metal cells, poly(anthraquinonyl) sulfide (PAQs) achieved higher energy density given the higher specific capacity (albeit proceeding as well through partial ion-paired and solvated cations, with thus true metrics being lower) yet operating at a significantly lower potential of about 1 V below that of Ca–Zn–PTtSA.[50] This positions Ca–Zn–PTtSA as a superior candidate for large energy storage applications, thanks to its higher energy efficiency driven by its higher operating voltage and low hysteresis.

Conclusions and outlook

In summary, the family of DI–M–PTtSA coordination polymers is shown to efficiently and reversibly store Mg^{2+}, Ca^{2+}, and Zn^{2+}

divalent cations with current practical relevance, while equally performing for the so far not explored electrochemical storage of Sr^{2+} and even Ba^{2+}, confirming their universality for divalent cation storage. The Sr^{2+} and Ba^{2+} analogues stand out as the only materials capable of reversibly releasing and storing Sr^{2+} and Ba^{2+}, while Ca–Zn–PTtSA is identified as the only prepared Ca-ion containing positive electrode material which is stable under ambient air conditions. The Mg/Ca–Zn–PTtSA materials perform effectively as electrodes for Mg^{2+} and Ca^{2+} storage, offering a combination of high voltage, high rate, energy density, stability, and low voltage hysteresis, surpassing the state-of-the-art reported materials. Combined with straightforward synthesis and high sustainability, these materials mark a milestone in the design of electrode materials for divalent cation storage, overcoming most known associated challenges. Key insights for future divalent cation electrode materials include: (I) extended conjugation yields diffuse negative charge, reducing coulombic attraction with guest cations, enhancing migration rates and enabling redox activity of bare cations instead of solvated or ion paired forms and (II) traditional approaches focusing on crystalline materials hinder divalent ion mobility, leading to high activation energy of diffusion.[16] An amorphous framework leverages these insights,[53] reducing diffusion barriers and accelerating cation movement. This understanding of the composition–structure–property–performance relationship can guide the development of advanced divalent cation batteries.

These materials not only unlock the field of high voltage divalent containing materials but also emphasize now the need to develop higher anodic stability electrolytes compatible with Mg- and Ca-metal interfacial chemistry.[51,54,55] While operating at moderate voltages (3–3.6 V vs. Mg/Ca), our materials echo the early stages of Li and Na battery development, where the introduction of high-voltage positive electrode chemistries drove advancements in electrolyte formulations.[56,57] Unlike conventional Mg and Ca battery research, which has thus far prioritized compatibility with metal anodes, the DI–M–PTtSA CPs challenge the overlooked aspect of anodic stability by presenting the high-voltage positive electrode chemistries for divalent systems. Rather than a limitation, the current anodic stability gap presents an opportunity to propel transformative developments in high-voltage electrolytes, enabling breakthroughs in Mg and Ca energy storage technologies. As cation-reservoir materials, these coordination polymers represent promising candidates for enabling an anode-free configuration in divalent metal batteries. Although such configurations were not demonstrated in this work, their favorable ion storage behavior suggests potential for future exploration. When combined with high-voltage-stable electrolytes, this approach could contribute to the development of practical, high-energy divalent battery systems.

Author contributions

R. M., X. G., J. W. and A. V. conceived and designed the experiments. R. M., X. G., J. W., P. A. and D. R. synthesized and fabricated organic electrodes. R. M., X. G., J. W., P. A., D. R., D. M., M. D., D. T., R. D, and X. L. performed electrochemical and materials characterization. O. L., T. P., and J. B. performed characterization in metal cells. A. B., L. S. and A. P. conducted hard X-ray absorption spectroscopy measurements and analyses. K. R. carried out single-crystal X-ray diffraction measurements and analyses. X. G. drafted the initial manuscript, and all authors contributed to reviewing and editing the manuscript. J. W., A. P., J. B., J. F. G. and A. V. supervised the project and acquired the funding.

Conflicts of interest

The authors declare no competing interests.

Data availability

The data that support the findings of this study are available from the corresponding author upon reasonable request.

Supplementary information is available. See DOI: **https://doi.org/10.1039/d5ee02567b**.

Acknowledgements

9122 | Energy Environ. Sci., 2025, 18, 9114–9124

This journal is © The Royal Society of Chemistry 2025

References

1 M. Armand and J.-M. Tarascon, Building better batteries, *Nature*, 2008, **451**, 652–657.

2 Y. Chen, K. Fan, Y. Gao and C. Wang, Challenges and perspectives of organic multivalent metal-ion batteries, *Adv. Mater.*, 2022, **34**, 2200662.

3 T. D. Gregory, R. J. Hoffman and R. C. Winterton, Nonaqueous electrochemistry of magnesium: applications to energy storage, *J. Electrochem. Soc.*, 1990, **137**, 775.

4 D. R. Lide, *CRC handbook of chemistry and physics*, CRC Press, 2004, vol. 85.

5 Z. P. Energy and S. Power, Time for lithium-ion alternatives, *Nat. Energy*, 2022, **7**, 461.

6 A. Ponrouch, *et al.*, Multivalent rechargeable batteries, *Energy Storage Mater.*, 2019, **20**, 253–262.

7 M. Matsui, Study on electrochemically deposited Mg metal, *J. Power Sources*, 2011, **196**, 7048–7055.

8 J. D. Forero-Saboya, D. S. Tchitchekova, P. Johansson, M. R. Palacín and A. Ponrouch, Interfaces and interphases in Ca and Mg batteries, *Adv. Mater. Interfaces*, 2022, **9**, 2101578.

9 S. D. Pu, *et al.*, Current-density-dependent electroplating in Ca electrolytes: From globules to dendrites, *ACS Energy Lett.*, 2020, **5**, 2283–2290.

10 M. Mao, T. Gao, S. Hou and C. Wang, A critical review of cathodes for rechargeable Mg batteries, *Chem. Soc. Rev.*, 2018, **47**, 8804–8841.

11 Y. Liang, H. Dong, D. Aurbach and Y. Yao, Current status and future directions of multivalent metal-ion batteries, *Nat. Energy*, 2020, **5**, 646–656.

12 Y. Zheng, *et al.*, Magnesium cobalt silicate materials for reversible magnesium ion storage, *Electrochim. Acta*, 2012, **66**, 75–81.

13 Z.-D. Huang, *et al.*, MgFePO$_4$F as a feasible cathode material for magnesium batteries, *J. Mater. Chem. A*, 2014, **2**, 11578–11582.

14 L. Folco and M. Mellini, Crystal chemistry of meteoritic kirschsteinite, *Eur. J. Mineral.*, 1997, **9**, 969–973.

15 A. Torres, F. Luque, J. Tortajada and M. Arroyo-de Dompablo, Analysis of minerals as electrode materials for Ca-based rechargeable batteries, *Sci. Rep.*, 2019, **9**, 9644.

16 P. Canepa, *et al.*, Odyssey of multivalent cathode materials: open questions and future challenges, *Chem. Rev.*, 2017, **117**, 4287–4341.

17 T. R. Juran, J. Young and M. Smeu, Density functional theory modeling of MnO$_2$ polymorphs as cathodes for multivalent ion batteries, *J. Phys. Chem. C*, 2018, **122**, 8788–8795.

18 S. Kim, *et al.*, High-voltage phosphate cathodes for rechargeable Ca-ion batteries, *ACS Energy Lett.*, 2020, **5**, 3203–3211.

19 R. Zhang and C. Ling, Unveil the chemistry of olivine FePO4 as magnesium battery cathode, *ACS Appl. Mater. Interfaces*, 2016, **8**, 18018–18026.

20 C. Kim, *et al.*, Direct observation of reversible magnesium ion intercalation into a spinel oxide host, *Adv. Mater.*, 2015, **27**, 3377–3384.

21 B. Pan, *et al.*, Advanced hybrid battery with a magnesium metal anode and a spinel LiMn$_2$O$_4$ cathode, *Chem. Commun.*, 2016, **52**, 9961–9964.

22 M. Cabello, *et al.*, Advancing towards a veritable calcium-ion battery: CaCo$_2$O$_4$ positive electrode material, *Electrochem. Commun.*, 2016, **67**, 59–64.

23 M. Cabello, *et al.*, Applicability of molybdite as an electrode material in calcium batteries: a structural study of layer-type Ca$_x$MoO$_3$, *Chem. Mater.*, 2018, **30**, 5853–5861.

24 Z. Rong, *et al.*, Materials design rules for multivalent ion mobility in intercalation structures, *Chem. Mater.*, 2015, **27**, 6016–6021.

25 Z. Li, *et al.*, Fast kinetics of multivalent intercalation chemistry enabled by solvated magnesium-ions into self-established metallic layered materials, *Nat. Commun.*, 2018, **9**, 5115.

26 J. Wang, *et al.*, Conjugated sulfonamides as a class of organic lithium-ion positive electrodes, *Nat. Mater.*, 2021, **20**, 665–673.

27 J. Wang, *et al.*, A high-voltage organic framework for high-performance Na-and K-ion batteries, *ACS Energy Lett.*, 2022, **7**, 668–674.

28 J. Wang, *et al.*, High performance Li-, Na-, and K-ion storage in electrically conducting coordination polymers, *Energy Environ. Sci.*, 2022, **15**, 3923–3932.

29 J. Wei, *et al.*, Supramolecule-based excluded-volume electrolytes and conjugated sulfonamide cathodes for high-voltage and long-cycling aqueous zinc-ion batteries, *ACS Energy Lett.*, 2022, **8**, 762–771.

30 X. Fan, *et al.*, A universal organic cathode for ultrafast lithium and multivalent metal batteries, *Angew. Chem., Int. Ed.*, 2018, **57**, 7146–7150.

31 H. Dong, *et al.*, High-power Mg batteries enabled by heterogeneous enolization redox chemistry and weakly coordinating electrolytes, *Nat. Energy*, 2020, **5**, 1043–1050.

32 H. Dong, *et al.*, Directing Mg-storage chemistry in organic polymers toward high-energy Mg batteries, *Joule*, 2019, **3**, 782–793.

33 J. Bitenc, A. Vizintin, J. Grdadolnik and R. Dominko, Tracking electrochemical reactions inside organic electrodes by operando IR spectroscopy, *Energy Storage Mater.*, 2019, **21**, 347–353.

34 T. Bashir, *et al.*, Progress in 3D-MXene electrodes for lithium/sodium/potassium/magnesium/zinc/aluminum-ion batteries, *Electrochem. Energy Rev.*, 2023, **6**, 5.

35 V. Martin-Diaconescu, *et al.*, Ca K-edge XAS as a probe of calcium centers in complex systems, *Inorg. Chem.*, 2015, **54**, 1283–1292.

36 J. Wang, *et al.*, CaV$_6$O$_{16}$·2.8H$_2$O with Ca^{2+} Pillar and Water Lubrication as a High-Rate and Long-Life Cathode Material for Ca-Ion Batteries, *Adv. Funct. Mater.*, 2022, **32**, 2113030.

37 D. S. Tchitchekova, *et al.*, Electrochemical calcium extraction from 1D-Ca$_3$Co$_2$O$_6$, *Dalton Trans.*, 2018, **47**, 11298–11302.

38 S. Gu, *et al.*, Preparation of MgCo$_2$O$_4$/graphite composites as cathode materials for magnesium-ion batteries, *J. Solid State Electrochem.*, 2019, **23**, 1399–1407.

This journal is © The Royal Society of Chemistry 2025

Energy Environ. Sci., 2025, **18**, 9114–9124 | **9123**

39 J. Zeng, *et al.*, A promising high-voltage cathode material based on mesoporous $Na_3V_2(PO_4)_3$/C for rechargeable magnesium batteries, *Chem. – Eur. J.*, 2017, **23**, 16898–16905.

40 Z.-L. Xu, *et al.*, A new high-voltage calcium intercalation host for ultra-stable and high-power calcium rechargeable batteries, *Nat. Commun.*, 2021, **12**, 3369.

41 C. Chen, F. Shi, S. Zhang, Y. Su and Z. L. Xu, Ultrastable and high energy calcium rechargeable batteries enabled by calcium intercalation in a nasicon cathode, *Small*, 2022, **18**, 2107853.

42 Y. Zhu, *et al.*, Hydrated $Mg_xV_5O_{12}$ cathode with improved Mg^{2+} storage performance, *Adv. Energy Mater.*, 2020, **10**, 2002128.

43 S. Zhang, *et al.*, Poly(anthraquinonyl sulfide)/CNT composites as high-rate-performance cathodes for nonaqueous rechargeable calcium-ion batteries, *Adv. Sci.*, 2022, **9**, 2200397.

44 R. Verrelli, *et al.*, On the strange case of divalent ions intercalation in V_2O_5, *J. Power Sources*, 2018, **407**, 162–172.

45 C. Zhang, *et al.*, Tailoring the linking patterns of polypyrene cathodes for high-performance aqueous Zn dual-ion batteries, *Energy Environ. Sci.*, 2021, **14**, 462–472.

46 J. Li, C. Han, X. Ou and Y. Tang, Concentrated electrolyte for high-performance Ca-ion battery based on organic anode and graphite cathode, *Angew. Chem.*, 2022, **134**, e202116668.

47 L. Geng, *et al.*, Crystal structure transformation in Chevrel phase Mo_6S_8 induced by aluminum intercalation, *Chem. Mater.*, 2018, **30**, 8420–8425.

48 L. F. Wan, B. R. Perdue, C. A. Apblett and D. Prendergast, Mg desolvation and intercalation mechanism at the Mo6S8 chevrel phase surface, *Chem. Mater.*, 2015, **27**, 5932–5940.

49 M. Wang, *et al.*, The restructuring-induced CoO_x catalyst for electrochemical water splitting, *JACS Au*, 2021, **1**, 2216–2223.

50 J. Bitenc, *et al.*, Electrochemical performance and mechanism of calcium metal–organic battery, *Batteries Supercaps*, 2021, **4**, 214–220.

51 R. Mohtadi, O. Tutusaus, T. S. Arthur, Z. Zhao-Karger and M. Fichtner, The metamorphosis of rechargeable magnesium batteries, *Joule*, 2021, **5**, 581–617.

52 B. Pan, *et al.*, Polyanthraquinone-Based Organic Cathode for High-Performance Rechargeable Magnesium-Ion Batteries, *Adv. Energy Mater.*, 2016, **6**, 1600140.

53 Y. Orikasa, *et al.*, Noncrystalline nanocomposites as a remedy for the low diffusivity of multivalent ions in battery cathodes, *Chem. Mater.*, 2020, **32**, 1011–1021.

54 S. Hou, *et al.*, Solvation sheath reorganization enables divalent metal batteries with fast interfacial charge transfer kinetics, *Science*, 2021, **374**, 172–178.

55 R. Attias, M. Salama, B. Hirsch, Y. Goffer and D. Aurbach, Anode-electrolyte interfaces in secondary magnesium batteries, *Joule*, 2019, **3**, 27–52.

56 X. Zhang, *et al.*, A dicarbonate solvent electrolyte for high performance 5 V-Class Lithium-based batteries, *Nat. Commun.*, 2024, **15**, 536.

57 Y. Jin, *et al.*, Low-solvation electrolytes for high-voltage sodium-ion batteries, *Nat. Energy*, 2022, **7**, 718–725.

9124 | *Energy Environ. Sci.*, 2025, **18**, 9114–9124

This journal is © The Royal Society of Chemistry 2025